Supporting Information

# Mechanochemical Synthesis of Carbon Nanothread Single Crystals

Xiang Li,[1,2] Maria Baldini,[3] Tao Wang,[2,4] Bo Chen,[5] En-shi Xu,[2,4] Brian Vermilyea,[2,4] Vincent H. Crespi,[1,2,4,6] Roald Hoffmann,[5] Jamie J. Molaison,[7] Christopher A. Tulk,[7] Malcolm Guthrie,[8] Stanislav Sinogeikin,[9] John V. Badding[1,2,4,6]*

[1]Department of Chemistry, Pennsylvania State University, University Park, PA 16802, USA

[2]Materials Research Institute, Pennsylvania State University, University Park, PA 16802, USA

[3]Geophysical Laboratory, Carnegie Institution of Washington, Advanced Photon Source, Argonne National Laboratory, Argonne, IL 60439, USA

[4]Department of Physics, Pennsylvania State University, University Park, PA 16802, USA

[5]Department of Chemistry and Chemical Biology, Cornell University, Baker Laboratory, Ithaca, NY 14853-1301, USA

[6]Department of Materials Science and Engineering, Pennsylvania State University, University Park, PA 16802, USA

[7]Neutron Sciences Directorate, Oak Ridge National Laboratory, Oak Ridge, TN 37830, USA

[8]European Spallation Source, ESS AB, SE-22100, Lund, Sweden

[9]High Pressure Collaborative Access Team, Geophysical Laboratory, Carnegie Institution of Washington, Argonne, IL 60439, USA

*Correspondence to: jbadding@chem.psu.edu

## 1. Materials and Methods

We used both benzene and perdeuterated benzene as reactants for syntheses in the Paris-Edinburgh press at the SNAP instrument at the Spallation Neutron Source. Benzene was frozen using liquid nitrogen to avoid evaporation and loaded into encapsulated TiZr gaskets; the dry nitrogen atmosphere from the liquid prevented condensation of water. The samples were placed into a VX3 Paris-Edinburgh press[1] equipped with double-toroid polycrystalline diamond anvils[2] and

compressed. The system was driven by an automatic hydraulic oil syringe pump, allowing controlled pressure ramps. The pressure-load calibration curve was obtained from in situ neutron diffraction. The sample pressure was approximately 23 GPa at the maximum oil pressure of 1,650 bar. The rates of compression are in the main text.

A symmetric diamond anvil cell with a 300 μm culet was used for in situ characterization at high pressure. Rhenium or stainless steel gaskets were indented to 40–50 μm thickness and a 100–110 μm diameter sample hole was drilled.[4] Pressure was determined in situ by ruby fluorescence. Liquid benzene was loaded into the gasket hole at room temperature. The cell was quickly closed to avoid evaporation and water contamination. Pure phase II single crystals were successfully synthesized in situ using resistive heating.[5] Two sets of gas membranes and digital gas controllers were employed to control the pressure rates precisely during both compression and decompression to reproduce PE cell synthesis conditions.

In-house X-ray diffraction data on the sample recovered from the Paris-Edinburgh press were collected with a 300 μm diameter, monochromatic copper Kα1 X-ray beam and a CCD area detector. In situ high–resolution high pressure X-ray diffraction measurements were conducted at beamline 16-ID-B at the Advanced Photon Source. A 30 keV 5×5 μm beam and both Pilatus 1M-F and Mar CCD area detectors were used for the powder and the single-crystal diffraction experiments. These two-dimensional diffraction patterns were reduced to one-dimensional patterns using Dioptas[6] to determine interplanar spacings vs. pressure. The only extraneous reflections observed in any of the in situ diffraction patterns were due to the diamond anvils; no diffraction from either the ruby pressure sensors or metal gaskets was observed.

Optical microscopy images were collected with an Olympus BX61 optical microscope with crossed polarizers and a sample rotation stage. *Ex situ* Raman spectra were measured using a Renishaw inVia microscope with 633 nm excitation. In situ high pressure Raman spectra were collected in a backscattering geometry using a custom confocal spectrometer with 660 nm laser excitation and type IIA ultrapure diamond anvils.

## 2. Modeling

To allow for multi-thread unit cells and possible structural disorder, initially sixteen-thread supercells were generated with hexagonal packing and either uniform or random thread azimuthal angles and axial positions, and then structurally relaxed using the AMBER molecular force field,[7] (which was best able to reproduce crystal structural data for known saturated hydrocarbons including diamondoids, see Table S1). For the uniform case, the final relaxed structures were re-relaxed within density functional theory at the PBE[8-10] level with empirical van der Waals interaction[11-12] (as implemented in VASP[13-16]). The differences between the empirical force field and density functional results for the ordered systems provide a rough measure of the degree of uncertainty in computational treatments of the non-bonded interactions that govern thread packing. All systems retain near-hexagonal symmetry. Achiral threads, even when initially disordered, consistently relax into single-thread unit cells with axial alignment in planes that shear relative to each other (Figure S14). Stiffchiral-1, also called polytwistane, tends to retain an initially disordered packing. The other three stiff chiral threads prefer to shear uniformly plane-by-plane for the initially ordered system, or to maintain irregular axial shifts for the initially disordered packing.

The packing geometries of nanothreads were examined in a rectangular sixteen-thread supercell, to accommodate possible ordered packing geometries with more than one thread per unit cell and also reasonable representations of packing disorder in the axial and/or azimuthal positions. In the ordered packed supercell, all 16 nanothreads initially have the same azimuthal angle and axial offset. For the disordered case, the azimuthal angles and axial positions of each thread are chosen from a uniform random distribution over 0 to $2\pi$ for azimuthal variation and the individual thread's *c*-axis periodicity for axial variation, and chiral threads were examined in both homochiral and racemic forms; in each case results were averaged over ten instances of disorder. To allow greater structural freedom during relaxation, the achiral nanothreads are extended in the axial direction to no less than 6 benzene formula units in the supercell. These ordered and disordered supercells were first examined at a classical MD level using the AMBER empirical potential, relaxing the structures with a force tolerance of $10^{-8}$ Kcal/mol/Å for achiral nanothreads, $10^{-3}$ Kcal/mol/Å for stiffchiral-1, -2, and-4 nanothreads and $10^{-2}$ Kcal/mol/Å for stiffchiral-3 nanothread, respectively. A less stringent (but still rigorous) tolerance was chosen for the chiral cases because of their larger unit cells. We could extract a fundamental repeat unit containing a

single nanothread with near-hexagonal lattice parameters from the fully relaxed supercells of the ordered packed nanothreads, which was then re-relaxed by first-principles density functional theory (DFT) using the PBE exchange correlation functional and PAW pseudopotential with energy cutoff of 700 eV, including the Van der Waals interaction in the DFT-D3 method with Becke-Jonson damping (validated in Table S1 against known saturated hydrocarbons) as implemented in the VASP package. Both atom positions and the unit cell shapes and volumes were relaxed using conjugate gradient. The initially ordered relaxed achiral threads tend to shift (shear) uniformly plane-by-plane to improve packing efficiency. The initial disordered achiral threads tend to relax to uniform azimuthal angles, but non-uniform axial shifts (upper row of Figure S14). For the thread stiffchiral-1, also called polytwistane, the inter-thread interaction as a function of their relative axial shift or azimuthal angle appears to be very smooth – no clear tendency to axial or azimuthal order is found (lower row of Figure S14); while the other three stiff chiral threads prefer to shear uniformly plane-by-plane for the initially ordered system, or to maintain irregular axial shifts in the initially disordered packing. For the "lumpier" chiral threads (stiffchiral-2, -3, and -4), the heterochiral (i.e. racemic) packings tend to be denser than the homochiral packings (Table S2) due to the more favorable contacts between helices of opposite chirality. None of the ordered outcomes have more than a single thread per unit cell. The inter-planar spacings for relaxed structures were obtained using CrystalDiffract, deriving the {100} hexagonal inter-planar spacings from the {400} planes of the supercell.

All the calculations for lattice constants were obtained at 0 K, while the experimental data were collected at room temperature. To compare these results, we made a rough estimate of the linear thermal expansion of nanothreads between 0 and 300K by considering the known linear thermal expansion coefficients of related systems: hexagonal graphite along the c-axis at 300K ($2.9\times10^{-5}$/K)[17], simple cubic fullerene at 261K ($6.2 \pm 0.2 \times10^{-5}$/ K),[17-18] adamantane phase I from 208–543K ($4.7\times10^{-4}$/ K)[19-21], and bicyclo[2.2.2] octane phase I from 164–447 K ($4.4\times10^{-4}$/ K).[19-21] These systems yield linear dimensional changes of 0.9%, 0.62%, 3–4%, 3–4%, respectively from 0 to 300K. Nanothread thermal expansion over a similar temperature range is thus estimated as in the range of 1–3%.

### 3. Compression of a Second Crystal Oriented Along the c-axis

Compression of a second benzene phase II single crystal neighboring the first one, which was oriented differently with its *c* axis [001] parallel to both the x-ray beam and load axis, revealed

no diffraction peaks characteristic of nanothreads for ω ±15°. Formation of nanothreads along the *c* axis cannot be completely ruled out in view of the limited range of reciprocal space sampled, but the benzene columns along the c-axis are staggered such that cycloaddition reactions to form nanothreads appear less likely.[22]

## 4. Supporting Figures

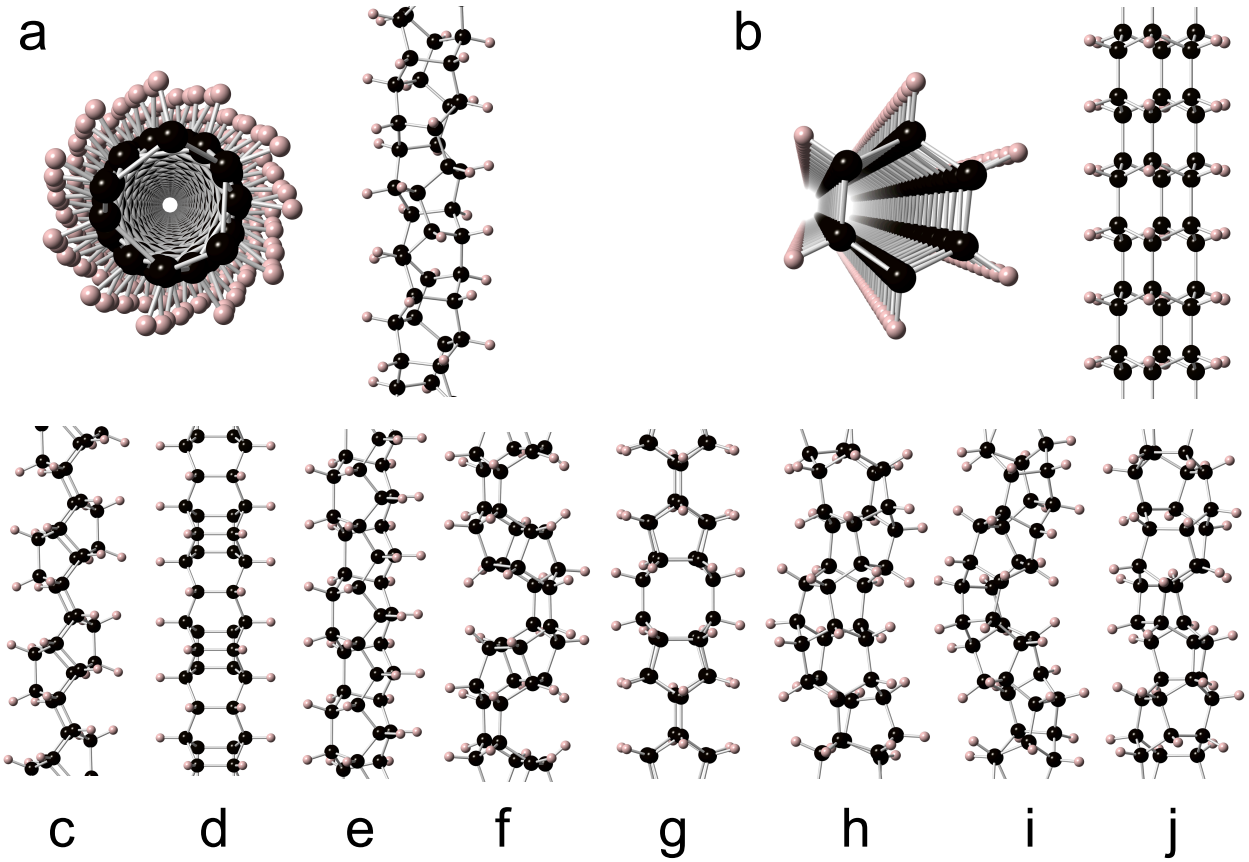


**Figure S1:**

**Candidate Nanothread Structures.** Nanothreads can be thought of as one-dimensional diamondoids with a $sp^3$ carbon core surrounded by hydrogens, as compared to "zero dimensional" diamondoids such as adamantine.[21] Their 1:1 C:H stoichiometry formula matches that of benzene. **(a)** Nanothread 143652 according to the nomenclature of reference,[23] also called stiffchiral-1, viewed down and perpendicular to thread axis. This structure is also called polytwistane in the literature.[24] **(b)** Nanothread 123456, also called tube (3,0) in the literature,[25] viewed down and perpendicular to the thread axis. Additional candidate nanothread structures: **(c)** Polymer I (135462);[26] **(d)** Achiral-4 (143562); **(e)** Achiral-6 (143562); **(f)** Achiral-3 (153624); **(g)** Achiral-5 (135462); **(h)** Stiffchiral-2 (136254); **(i)** Stiffchiral-3 (136425); **(j)** Stiffchiral-4 (135462). Relaxed structural coordinates of isolated nanothreads are provided in the supplementary material of E.-S. Xu *et al*..[23]

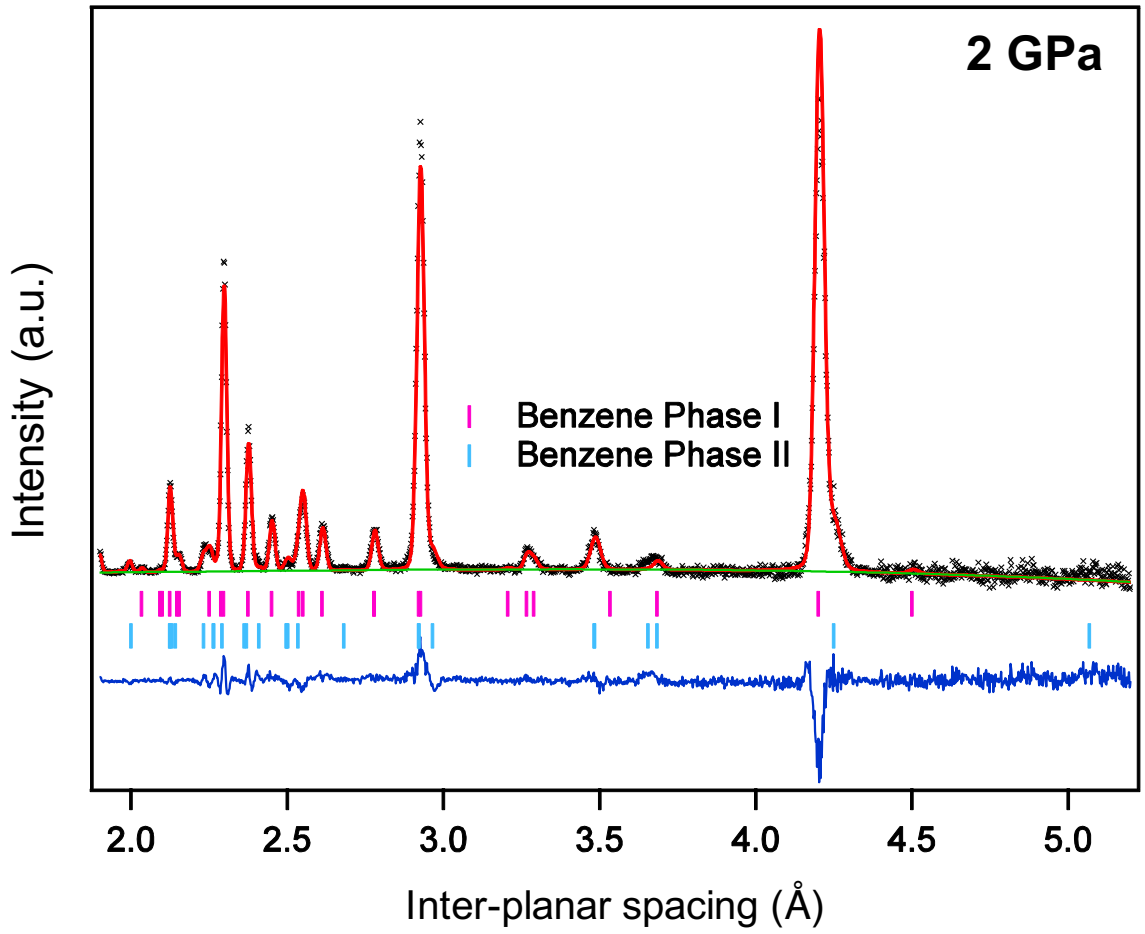


**Figure S2:**

**Neutron Diffraction Pattern of Benzene Phase I and Phase II Mixture at 2 GPa in a Paris-Edinburgh Press upon Increasing Pressure.** Unless annealed to high temperature (~300°C), molecular benzene above ~1.2 GPa at 20°C exists metastably in two solid phases,[5] orthorhombic phase I and monoclinic phase II. Both can be observed by in situ diffraction in both the Paris-Edinburgh press and the diamond anvil cell. This neutron diffraction pattern shows both phases co-existing in polycrystalline form. The red curve is a Pawley fit and the blue curve is the residual.

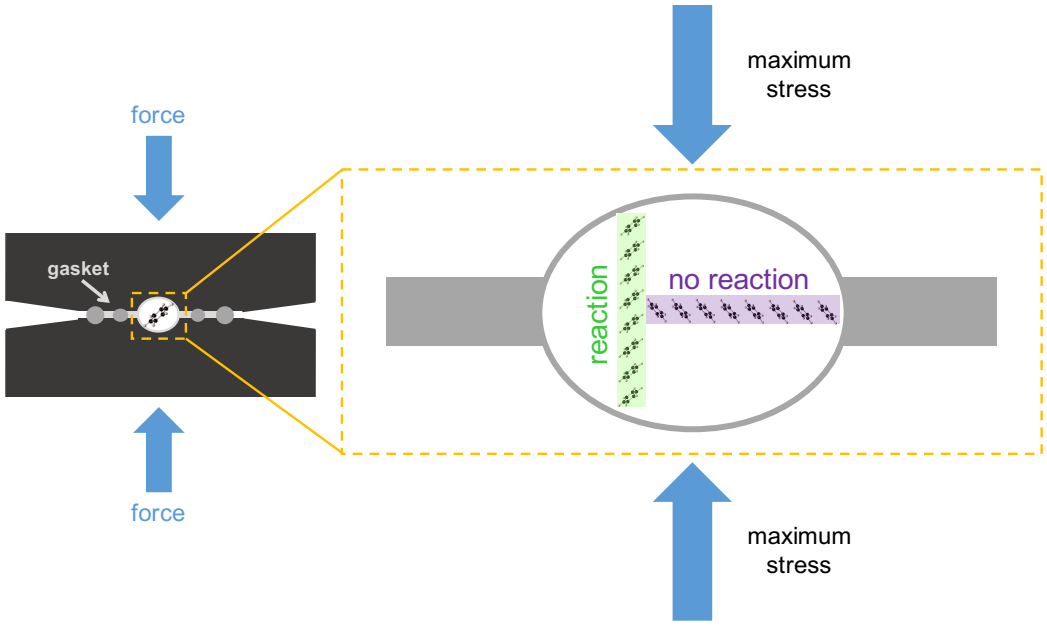


**Figure S3:**

**Unaxial Stress in the Paris-Edinburgh Press.** An additional stress component arises largely in the vertical direction of the applied load (blue arrows). This stress is typically uniaxial, i.e. larger in the vertical direction and symmetric in the horizontal plane. The magnitude of this stress component depends on the strength of the material under compression, but is often at least a few percent at ~20 GPa pressures. Benzene molecules in columns within the three-dimensional benzene phase II crystal structure that are aligned parallel to this stress will be closer together than those in columns that are not parallel at that pressure. It is thus natural to anticipate that reaction may occur first in the direction parallel to the applied stress, helping to explain why nanothreads are consistently oriented parallel to it.

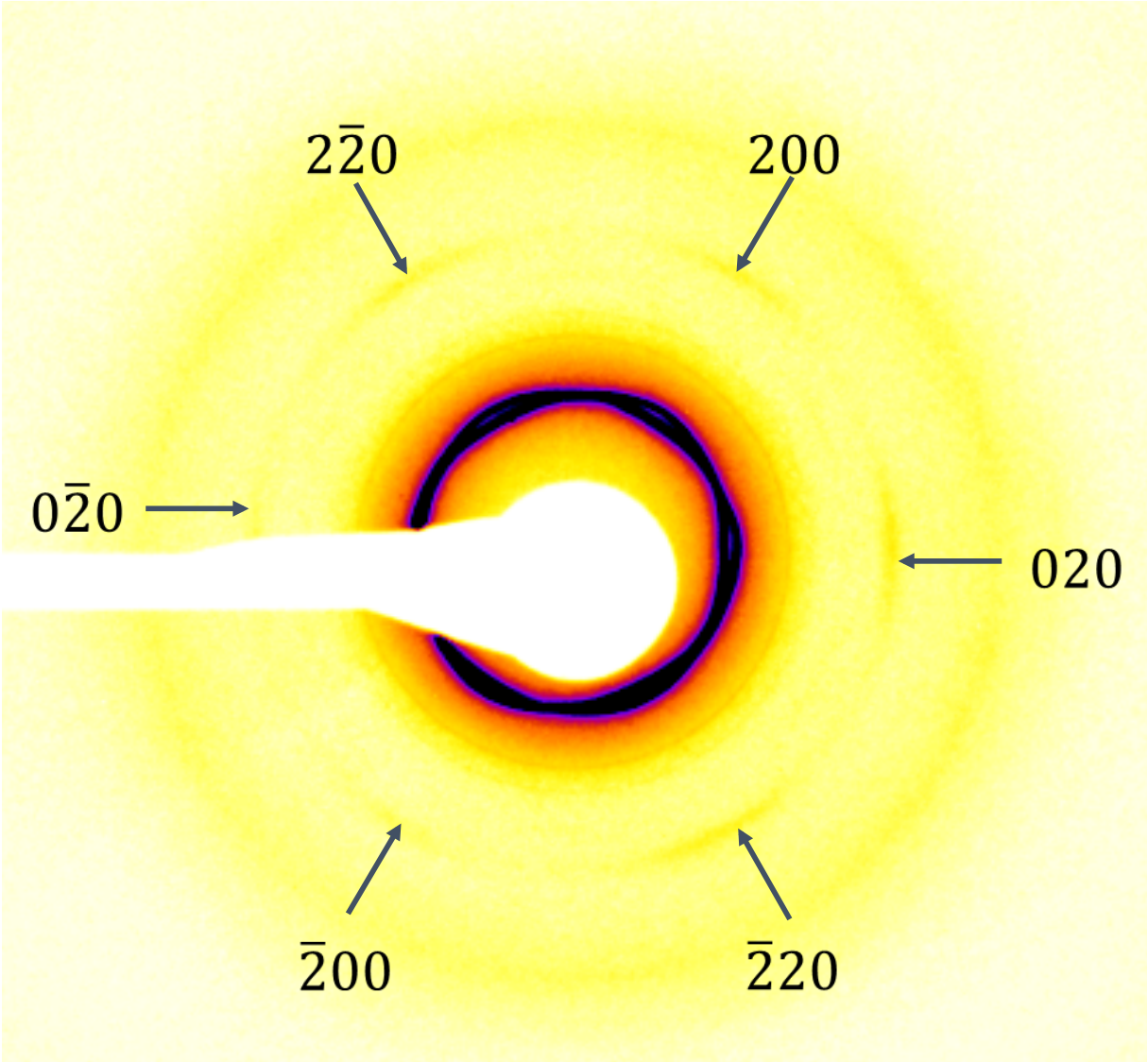


**Figure S4:**

**{200} Diffraction Arcs.** Weak {200} diffraction arcs (slightly darker yellow, marked with arrows) at $d$=2.76 Å are present when the {100} arcs are greatly overexposed (orange ring with bold black braids) for a sample synthesized in the Paris-Edinburgh (PE) cell from polycrystalline, multiphase benzene. Arcs are labeled arbitrarily according to the (hk0) indices expected for a hexagonal crystal diffracting along the [001] zone. The $0\bar{2}0$ reflection is largely but not completely hidden by the beam stop. The weakness of the {200} arcs is consistent with a rapid drop-off in form factor with increasing angle arising from the large size of the scattering objects, nanothreads, relative to atoms. Two very weak diffraction lines at $d$=4.10 Å, $d$=3.69 Å are also observed. We attribute these lines to a small amount of impurity phase. They can be distinguished from nanothread crystal diffraction features by their invariance to azimuthal angle.

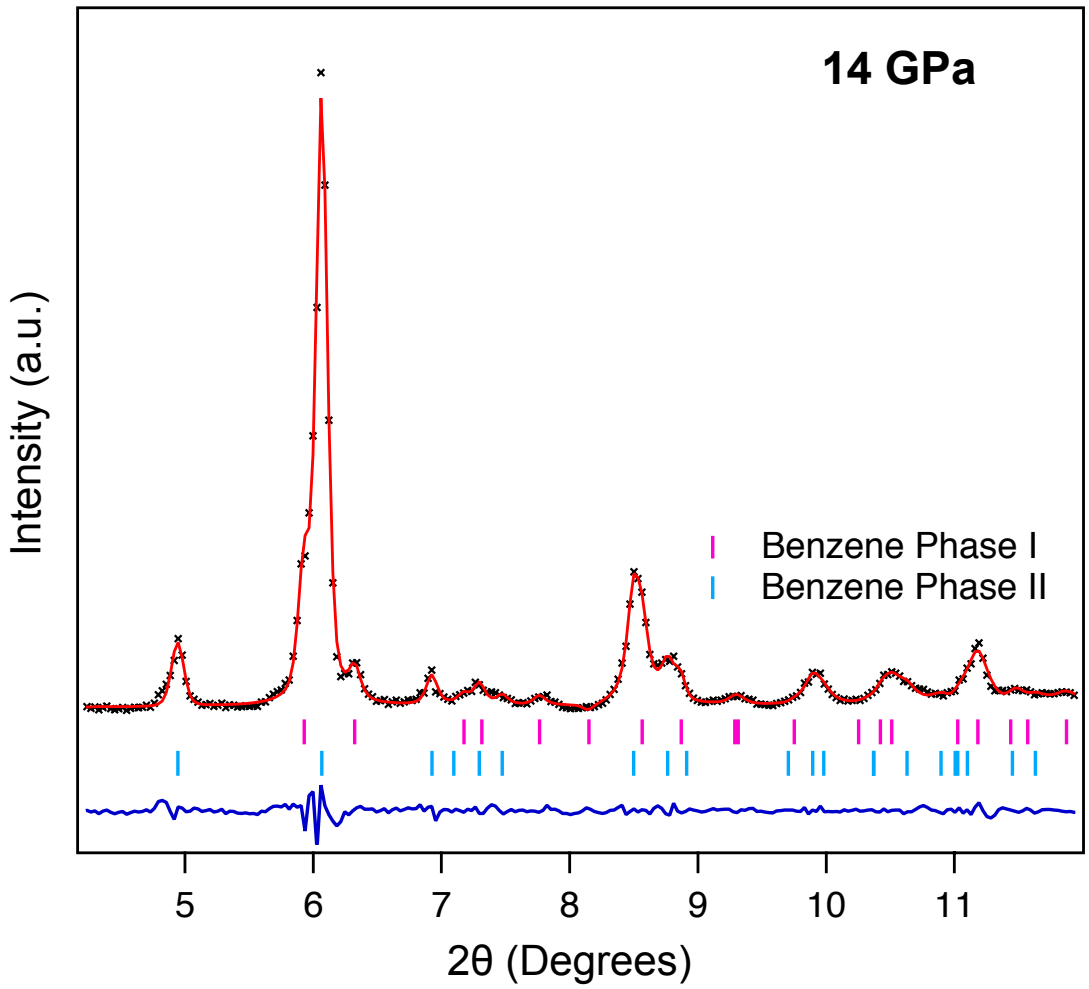


**Figure S5:**

**Synchrotron X-ray Diffraction Pattern of Benzene Phase I and Benzene Phase II Mixture at 14 GPa upon Increasing Pressure in a Diamond Anvil Cell.** Pawley fit[27] of the one-dimensional diffraction pattern for benzene upon compression to 14 GPa obtained by integrating the two-dimensional diffraction pattern. Both phase I (spacegroup Pbca) and phase II (spacegroup $P2_1/c$) are present at this pressure unless special care is taken to anneal away phase I. The red curve is the fit and the blue curve is the residual. Magenta and light blue short vertical lines indicate the expected positions of benzene phase I and phase II diffraction peaks, respectively.

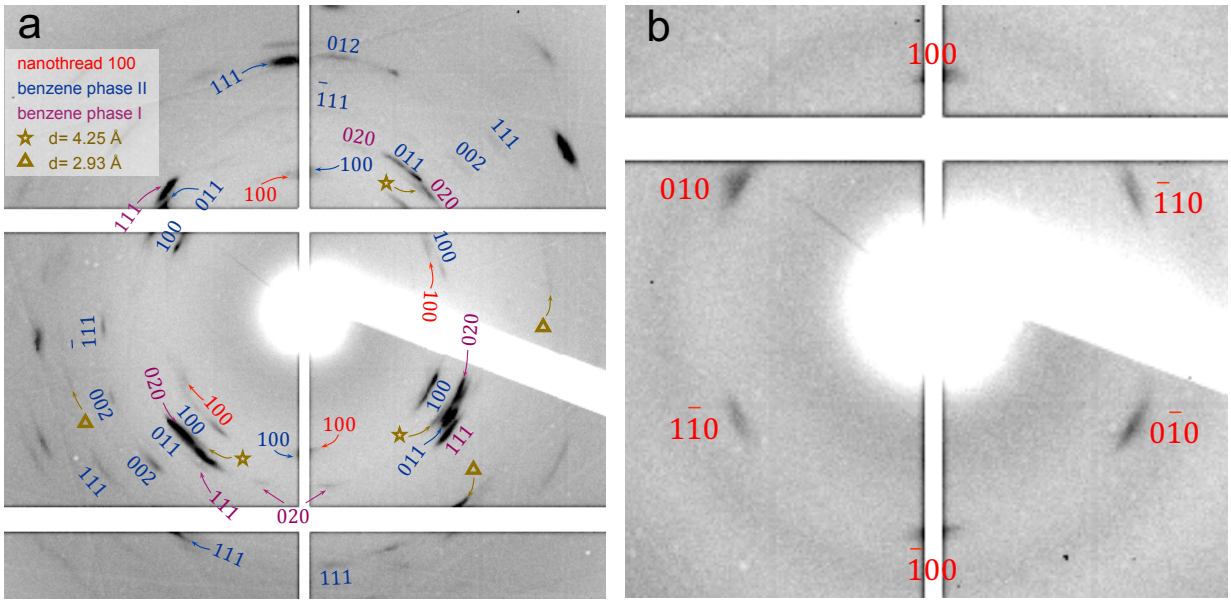


**Figure S6:**

**In situ Nanothread Diffraction at High Pressure**

**(a)** Diffraction pattern collected upon release of pressure to 3 GPa for the mixed phase-I/phase-II polycrystalline sample shows that both phases coexist in the sample volume that forms single crystal nanothreads upon release of pressure. Parentheses are not used in the (*hkl*) labels for brevity. The nanothread {100} arcs are labeled in red. Four of the six {100} arcs that remain in (b) are observed. Other diffraction arcs not indexable as phase-I or phase-II that disappear upon melting are labeled with stars and triangles. These arcs may be due to a Phase II′ phase, called phase III′ in early literature,[28] that was proposed and later questioned.[29] This structure would differ from phase II only slightly. **(b)** Diffraction pattern collected upon release of pressure to less than 0.1 GPa for the mixed phase-I/phase-II polycrystalline sample. Liquid benzene remains (faint broad ring). A six-fold symmetric diffraction pattern is the only crystalline feature remaining after the solid polycrystalline phase I and phase II benzene melts; it is characteristic of a nanothread single crystal with its hexagonal *c* axis zone parallel to the incident x-ray beam (and also the applied uniaxial stress).

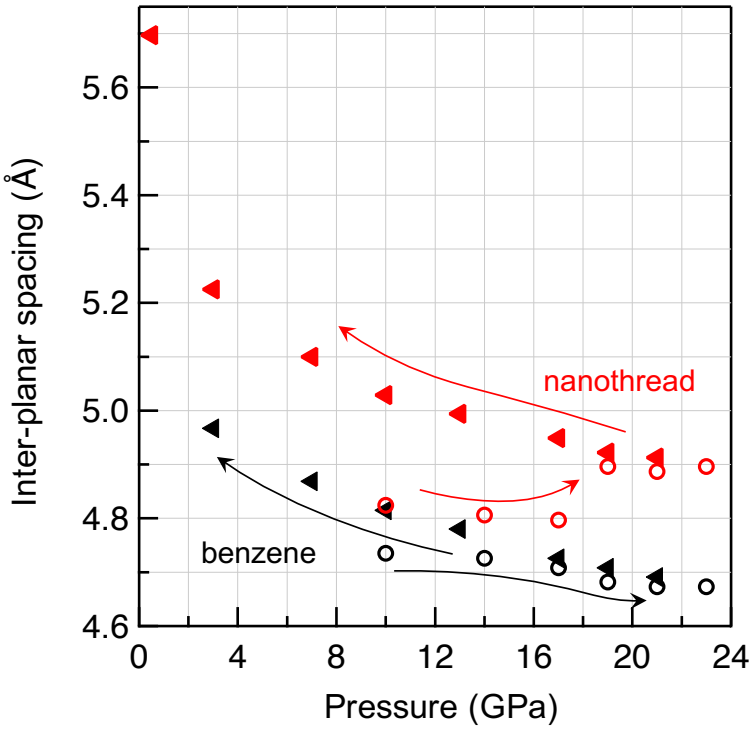


**Figure S7:**

**In situ Nanothread Diffraction at High Pressure**
Benzene phase II (100) and nanothread (100) interplanar spacings vs. pressure in increasing and decreasing pressure directions in a diamond anvil cell. Pressure is measured by ruby fluorescence. These diffraction planes are nearly parallel to both the incident x-ray beam and the axis of compression. They are thus impacted by the stress perpendicular to the axis of compression in the plane of the diamond culet. After the pressure is raised above ~1 GPa, the sample is a polycrystalline mixture of benzene phase I and phase II. In the increasing pressure direction benzene phase II (100) diffraction arcs (black open circles) exhibit a small discontinuity at 18 GPa, decreasing in interplanar spacing. New diffraction arcs at a slightly larger interplanar spacing than the benzene (100) ones also appear at 10 GPa in the increasing pressure direction (red open circles). It is not yet certain whether these arcs are associated with a nanothread reaction intermediate or nanothreads themselves. At 18 GPa there is a sudden *expansion* of these new arcs, which appears to be correlated with the reaction to form nanothreads. For example, at this pressure the sample also becomes photoluminescent (Figure S8). These arcs have an interplanar spacings characteristic of nanothreads. After this expansion at 18 GPa upon increasing pressure, the diffraction peaks can be traced up to 23 GPa and back to ambient pressure (solid red triangles) in the decreasing pressure direction. Upon release of pressure and melting of the solid benzene a six-fold symmetric diffraction pattern characteristic of nanothreads remains (Figure S6b). The benzene phase II (100) diffraction arcs in the decreasing pressure direction (solid black triangles) diverge at about 14 GPa from those in the increasing pressure direction such that there is hysteresis. It may be that after benzene has collapsed into nanothreads, there is slightly less stress in the plane perpendicular to the x-ray beam, which causes this hysteresis.

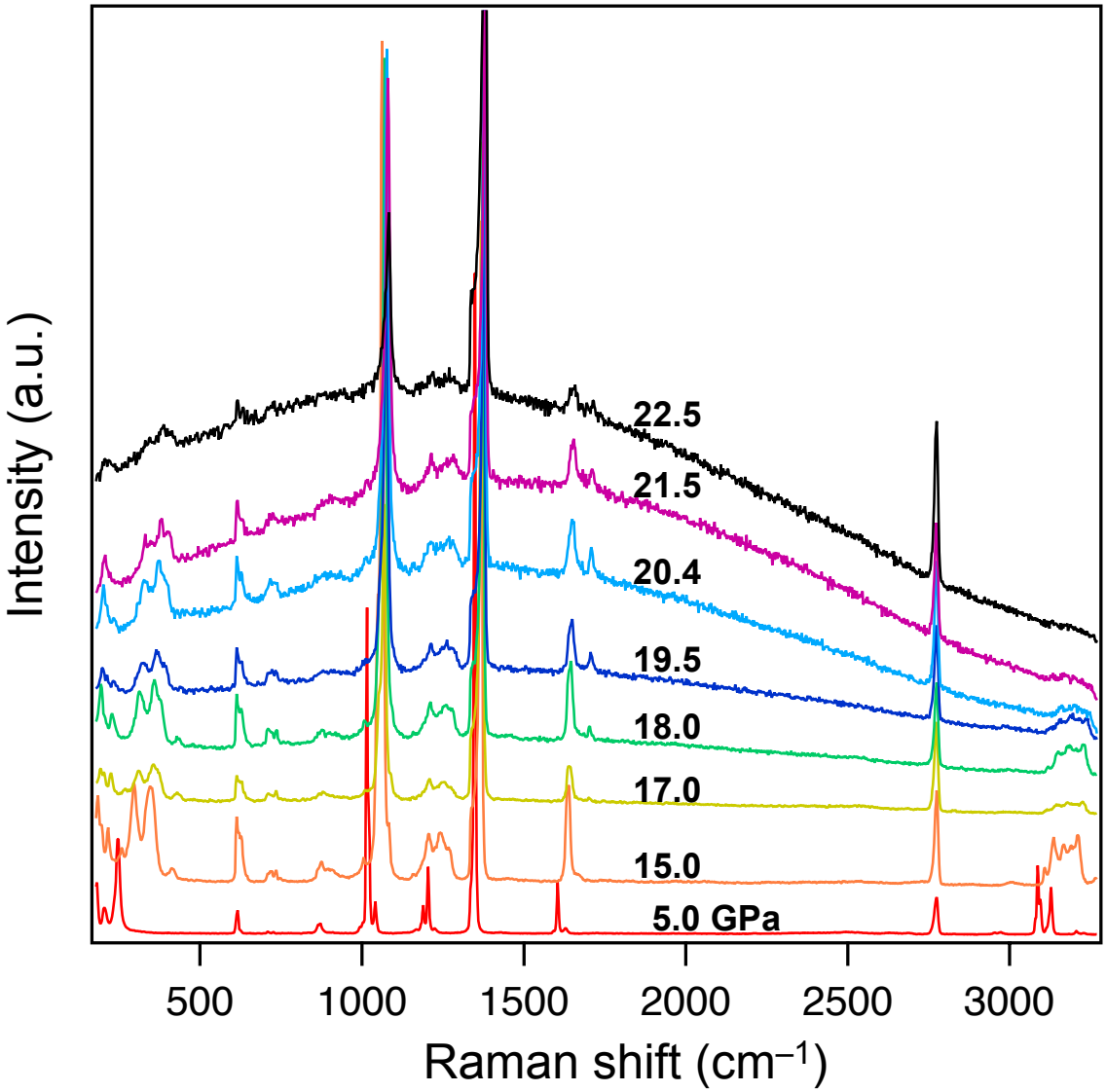


**Figure S8:**

**Raman Spectra of Benzene vs. Pressure during Compression.** An increase in background photoluminescence was observed in the Raman spectrum of polycrystalline, multiphase benzene when the pressure reached 19 GPa. The pressure at which the background increases correlates with the onset of new diffraction peaks associated with nanothread formation in the polycrystalline phase I/phase II samples. Prior investigations reported that oligomers of benzene formed after benzene was compressed to 16 GPa.[30] Thus the background here may arise from these relatively low molecular weight benzene oligomers. Benzene scattering and/or background photoluminescence make it difficult to observe nanothread Raman in situ at high pressure.

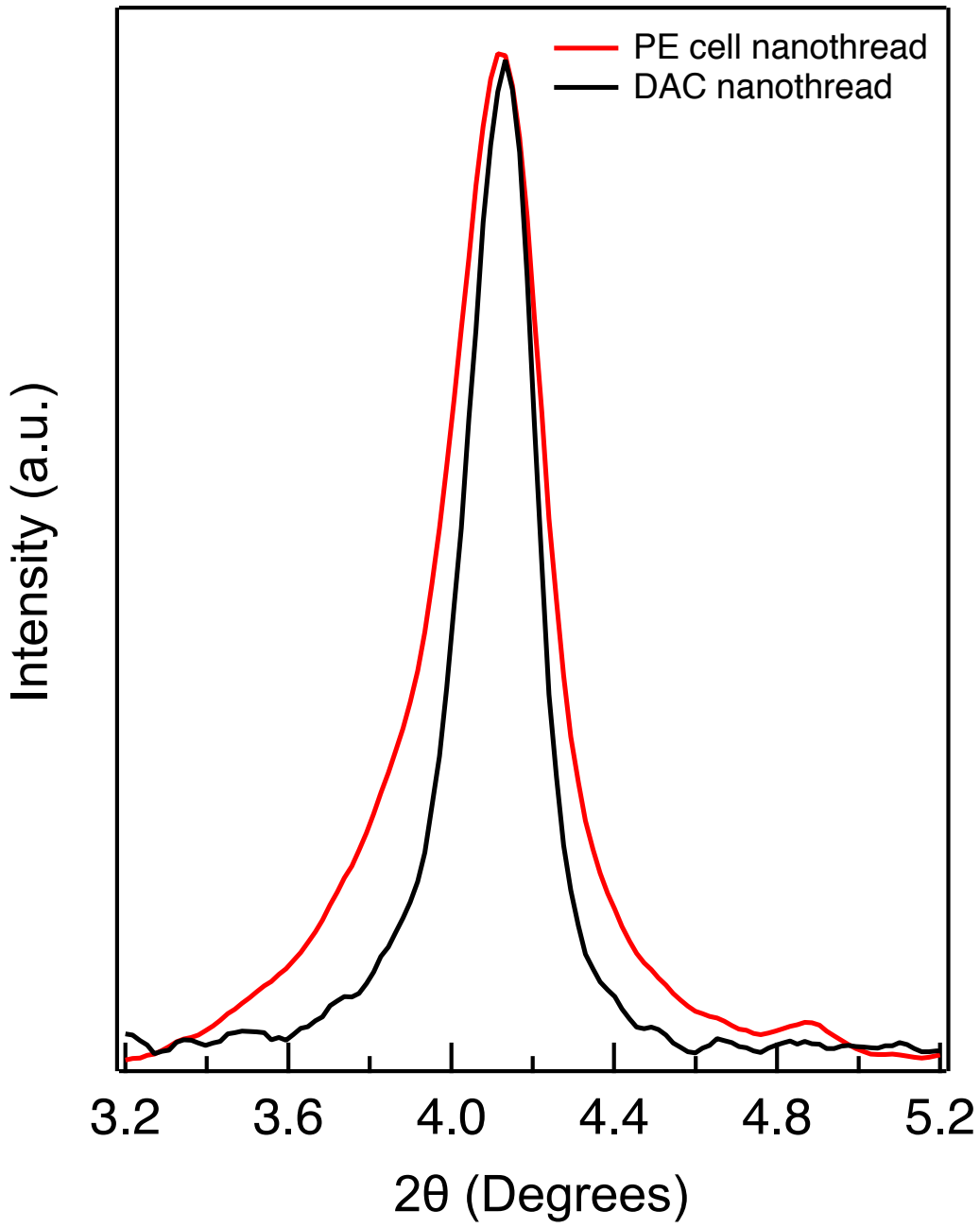


**Figure S9:**

**Comparision of Linewidths.** The full widths at half maximum for (100) reflections of nanothread samples synthesized from multiphase benzene in a Paris Edinburgh (PE) cell and a diamond anvil cell (DAC) are 0.280° and 0.206° 2θ respectively. The narrower linewidth for the sample synthesized in the DAC suggests more uniform packing, possibly arising from a difference in the uniaxial stress conditions inside the two types of pressure cells.

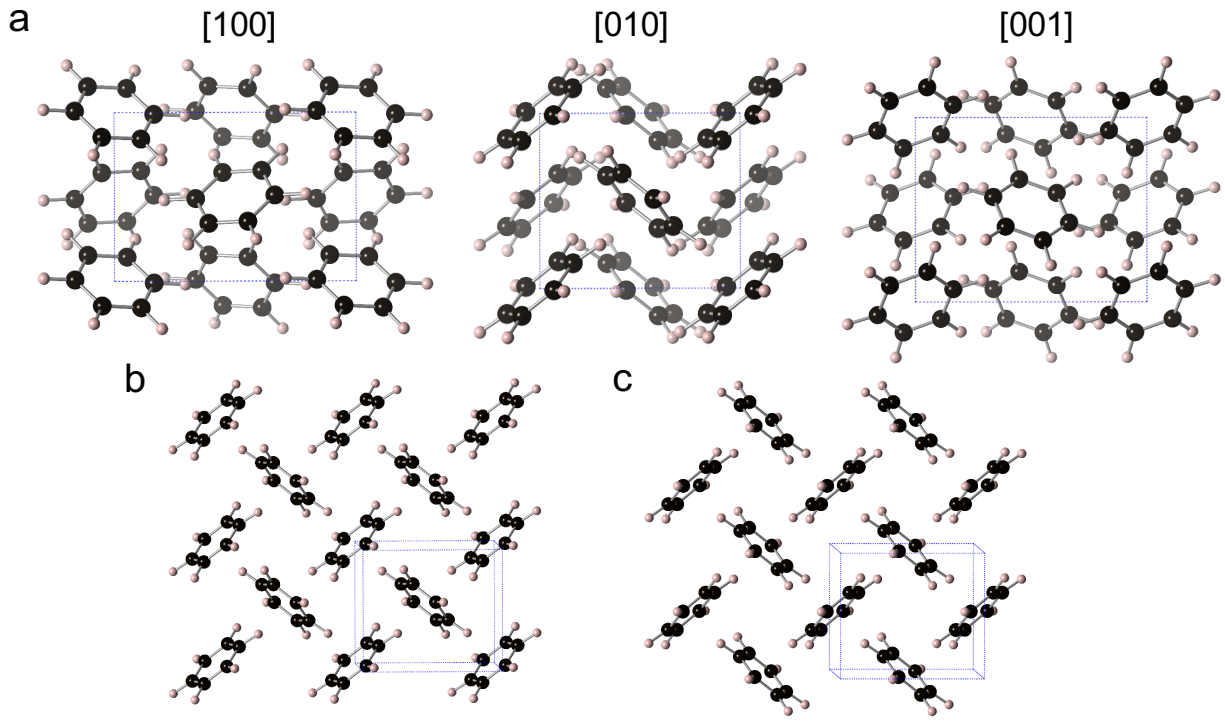


**Figure S10:**

**Benzene phase I (Pbca) structure calculated at 20 GPa.** (**a)** Views down *a* [100], *b* [010], and *c* [001] axes (*a*=6.37 Å, *b*=8.00 Å, *c*= 5.57 Å, $\alpha=\beta=\gamma=90^{\circ}$). This structure can be viewed as alternating layers of herringbone benzenes in the (010) and (020) planes stacked along the *b* axis. It was optimized at 20 GPa using the low-pressure crystal structure of Piermarini et. al.[5] as a starting point. **(b)** The layer in the (010) plane shows a herringbone arrangement of benzene molecules, where adjacent benzenes adopt an edge-to-face orientation. Such an edge-to-face orientation is not suitable for any C–C bond forming reaction, due to the lack of overlap between benzene π bonds. **(c)** The layer of herringbone-arranged benzenes in the (020) plane, with all benzene positions shifted half a unit cell along *c*, relative to the benzenes in the (010) plane. Because of this shift, adjacent benzenes from different layers are also in an orientation not suitable for any C–C bond forming reaction.

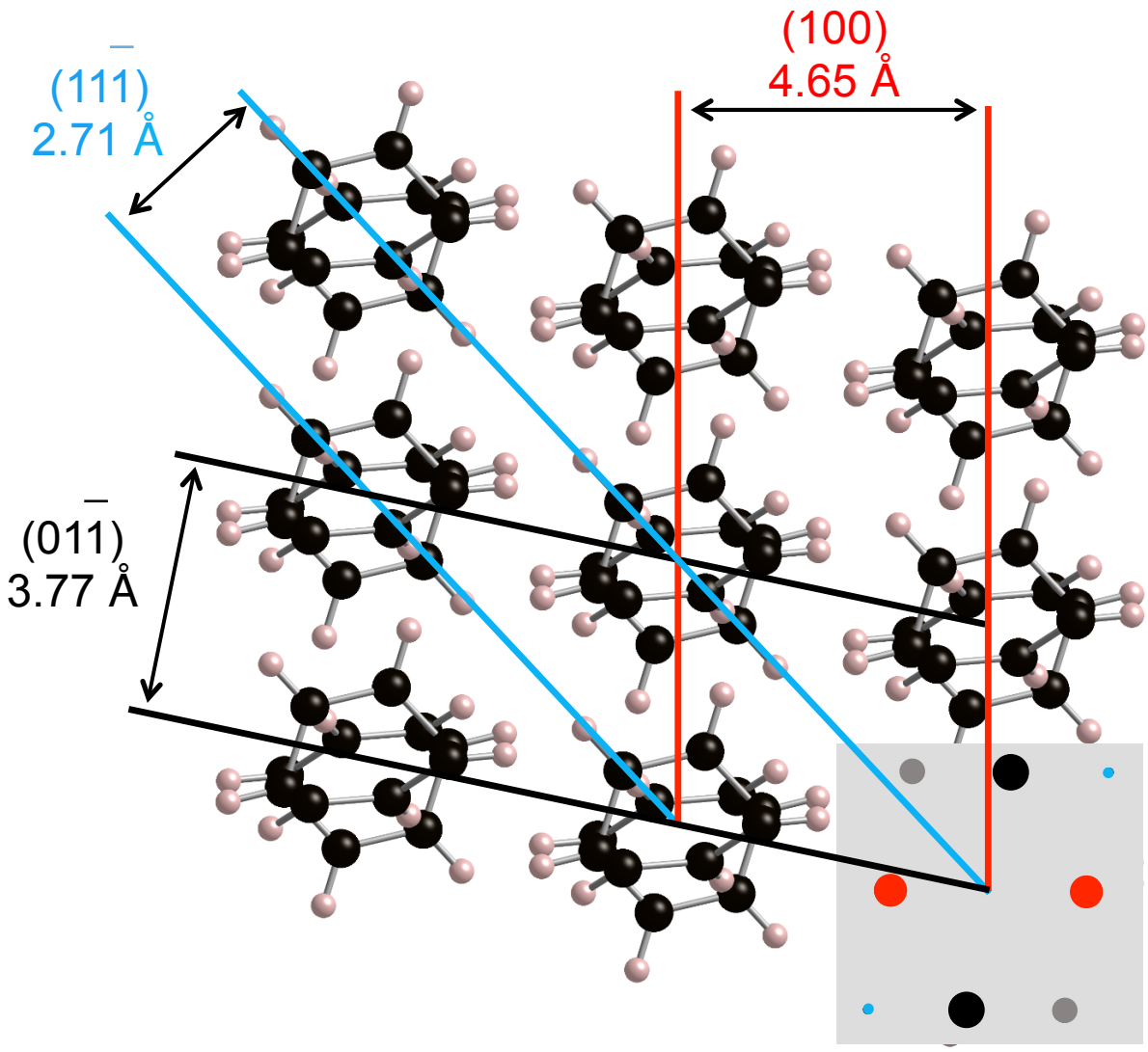


**Figure S11:**

**Monoclinic Phase II Benzene Crystal Viewed Down The [011] *b-c* Axis.** Some diffraction planes and their interplanar spacings at 23 GPa are shown, with the orientation and spacing of the corresponding diffraction spots in the inset. Diffraction planes for the grey spots are not shown. The smallest amount of expansion is needed for the (100) planes to form the psuedohex-agonal or hexagonal nanothread structure (Figure 4d). Other sets of planes such as the $(11\bar{1})$ and $(01\bar{1})$ must expand to a much larger extent. The *b-c* stacks have the columns with alternating orientations of benzene molecules different from the benzene columns along the *b* axis, which have uniform orientation. Both types of stacks are shown in Figure 4b. In contrast to the *b* stacks, the *b-c* stacks are not suited for [4+2] cycloaddition, but "*para* polymerization" starting with a diradical may be possible.[22] A pdb file of the benzene phase II coordinates is in the supporting information.

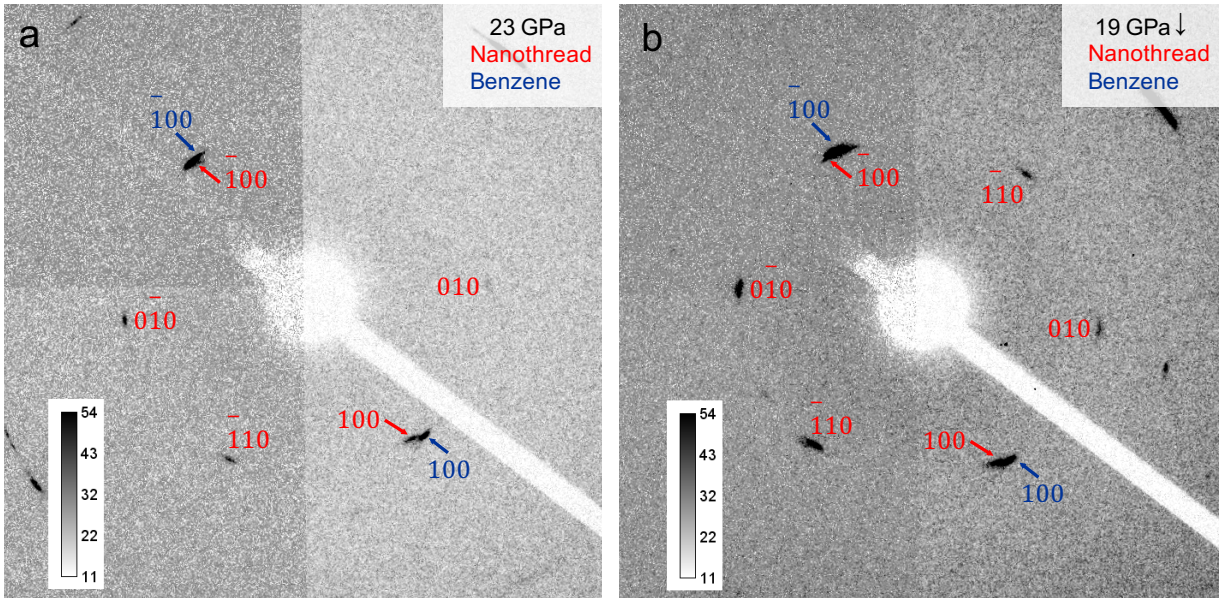


**Figure S12:**

**Diffraction Patterns of Nanothreads Synthesized from Single Crystals upon Decreasing Pressure Along [001] Zone Axis. (a)** Five of six nanothread reflections can be observed in a diffraction pattern at 23 GPa, along with the benzene (100) neighboring the nanothread (100) and the benzene ($\bar{1}$00) neighboring the nanothread ($\bar{1}$00). **(b)** Diffraction pattern at 19 GPa after reducing the pressure from 23 GPa. All six nanothread reflections can be observed and are somewhat more intense. The relative lower intensity observed for the two rightmost nanothread reflections is likely associated with a tilt away from the [001] zone axis, as these diffraction images were collected at the maximum ω angle of 15°. The increase of the reflection intensities as the pressure is reduced is likely associated either with more nanothread formation or better ordering of threads that have already formed.

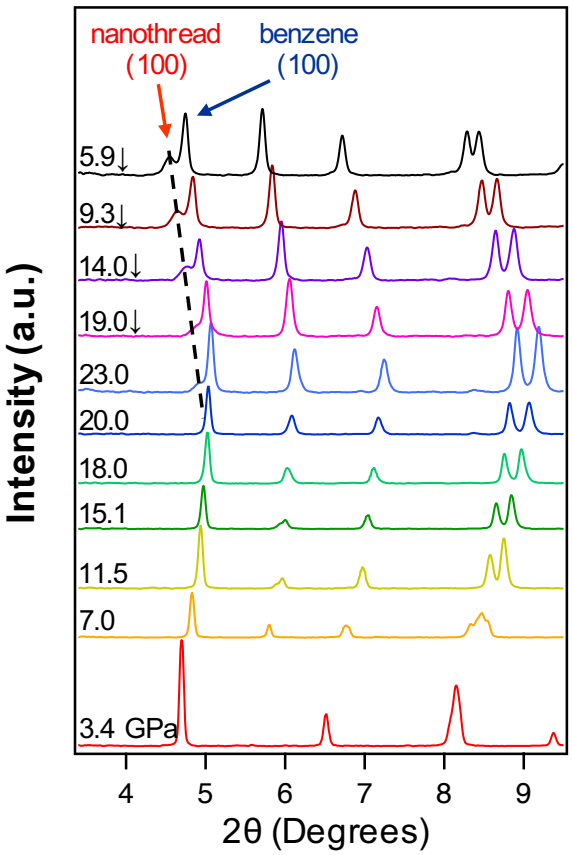


**Figure S13:**

**Evolution of Benzene and Nanothread Diffraction Patterns with Pressure.** One-dimensional diffraction patterns vs. pressure for the nanothread sample synthesized from pure single-crystal phase II benzene as a function of pressure. Down-arrows indicate decompression.

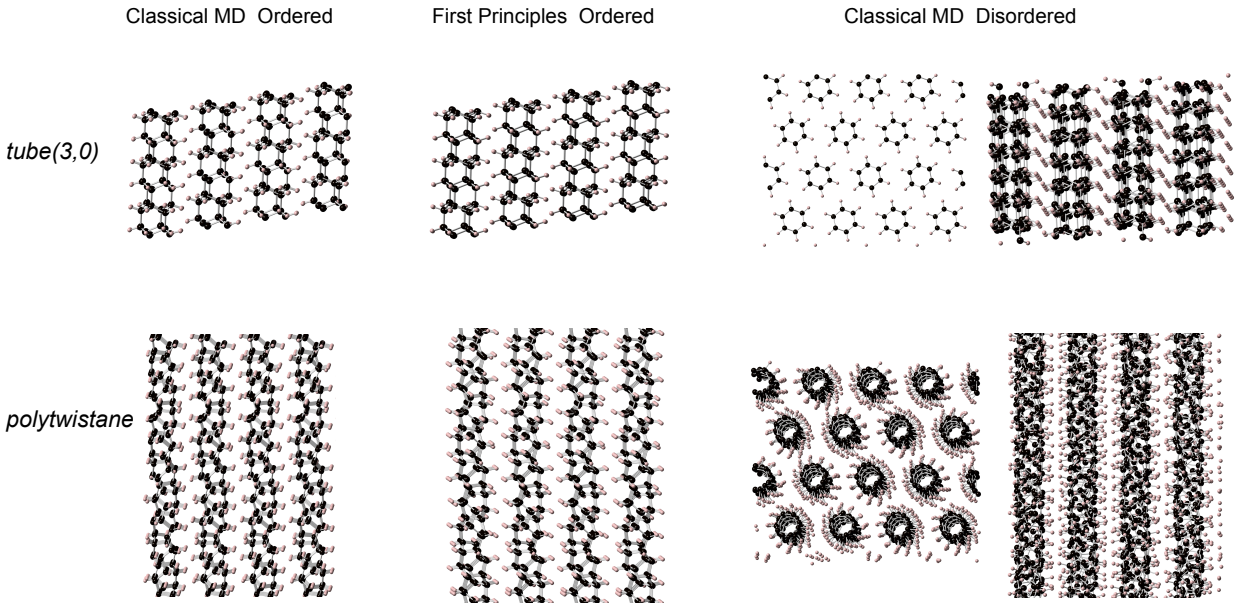


**Figure S14:**

**Optimized Packing Geometries of Achiral Tube (3,0) and Stiff Chiral Polytwistane.**
**Top:** Initially ordered achiral threads after structural relaxation using classical MD and first-principles density functional theory methods tend to shear axially plane-by-plane to improve packing efficiency. The initially disordered achiral threads relax to assume uniform azimuthal angles, but exhibit non-uniform axial shifts. **Bottom**: The relaxed structure of thread stiffchiral-1, also called polytwistane has no obvious pattern to the azimuthal angle (or equivalently, axial offsets) for either ordered or disordered initial conditions, whether homochiral or racemic.

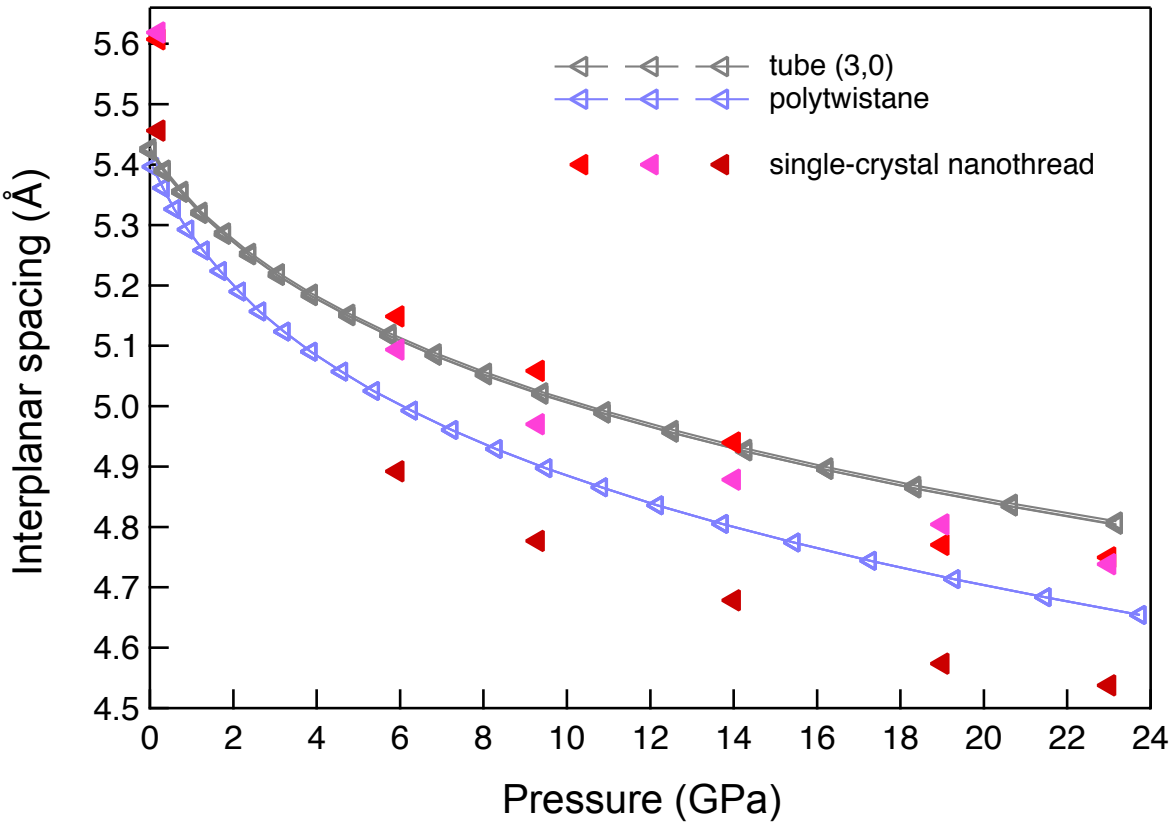


**Figure S15:**

**Inter-planar Spacing for Single-crystal Nanothreads Synthesized from Single Crystal Benzene Phase II and Calculated Results for Nanothreads Tube (3,0) and Polytwistane during Pressure Release from 24 GPa to Ambient Pressure.** The calculated lattice spacings of polytwistane under pressure are reasonably consistent with those of the synthesized single-crystal nanothreads after accounting for a 1–3% thermal expansion from the calculated case (0K) to the experimental conditions (300K). The calculated inter-planar spacings for both threads are nearly uniform for all {100} diffraction planes, whereas the experimental values have a moderate dispersion that may be related to anisotropic stress conditions within the experimental system, or possibly some admixture of a nanothread with a more pronounced deviation from cylindrical symmetry (e.g. degree 4). The somewhat higher compressibility of the experimental system at the lowest pressures may be related to slight imperfections in the thread packing that are squeezed out by modest pressures.

## 5. Supplementary Tables

**Table S1: DFT-D3 method and classical MD potential validation**

First-principles density functional theory including Van der Waals interaction (DFT-D3) and several empirical potentials have been validated against existing experimental results for various saturated hydrocarbon systems, including diamondoids that carry some of the key structural features of nanothreads. DFT-D3 and the AMBER force field overall reproduce most accurately key characteristics of saturated hydrocarbon molecular packing and therefore were chosen for detailed investigation of nanothread structural relaxation and packing optimization.

Adamantane ($C_{10}H_{16}$)

| Lattice | Exp | DFT_D3 | AMBER | REAX | COMPASS | DREIDING | EFF |
|---|---|---|---|---|---|---|---|
| *a* (Å) | 6.60 | 6.58 | 6.54 | 6.50 | 5.86 | 6.58 | 6.68 |
| *b* (Å) | 6.60 | 6.58 | 6.53 | 6.50 | 6.48 | 6.58 | 6.72 |
| *c* (Å) | 8.81 | 8.86 | 8.74 | 8.46 | 9.52 | 8.80 | 8.56 |

Iceane ($C_{12}H_{18}$)

| Lattice | Exp | DFT_D3 | AMBER | REAX | COMPASS | DREIDING | EFF |
|---|---|---|---|---|---|---|---|
| *a* (Å) | 6.58 | 6.52 | 6.45 | 6.27 | 6.45 | 6.45 | 6.77 |
| *b* (Å) | 6.58 | 6.65 | 6.47 | 6.27 | 7.47 | 6.49 | 6.48 |
| *c* (Å) | 11.84 | 11.74 | 11.22 | 11.03 | 11.48 | 11.24 | 10.97 |

Diamantane ($C_{14}H_{20}$)

| Lattice | Exp | DFT_D3 | AMBER | REAX | COMPASS | DREIDING | EFF |
|---|---|---|---|---|---|---|---|
| *a* (Å) | 10.11 | 10.08 | 9.97 | 9.78 | 9.71 | 9.99 | 10.10 |

Biadamantane ($C_{20}H_{30}$)

| Lattice | Exp | DFT_D3 | AMBER | REAX | COMPASS | DREIDING | EFF |
|---|---|---|---|---|---|---|---|
| *a* (Å) | 6.53 | 6.528 | 6.48 | 6.31 | 6.22 | 6.51 | 6.52 |
| *b* (Å) | 6.58 | 6.579 | 6.46 | 6.34 | 6.44 | 6.48 | 6.61 |
| *c* (Å) | 10.46 | 10.458 | 10.60 | 10.28 | 10.12 | 10.62 | 10.53 |
| $\alpha$ (°) | 87.50 | 87.500 | 87.11 | 89.51 | 91.25 | 87.07 | 87.36 |
| $\beta$ (°) | 104.58 | 104.579 | 105.97 | 103.93 | 99.90 | 106.10 | 104.43 |
| $\gamma$ (°) | 119.86 | 119.861 | 120.22 | 199.67 | 120.05 | 120.30 | 120.12 |

Benzene ($C_6H_6$)

| Lattice | Exp | DFT_D3 | AMBER | REAX | COMPASS | DREIDING |
|---|---|---|---|---|---|---|
| *a* (Å) | 7.29 | 7.24 | 6.34 | 6.71 | 4.99 | 7.21 |
| *b* (Å) | 9.47 | 9.49 | 9.01 | 9.17 | 9.34 | 9.39 |
| *c* (Å) | 6.74 | 6.82 | 7.62 | 6.15 | 5.45 | 6.87 |

Biapocamphane ($C_{18}H_{30}$)

| Lattice | Exp | DFT_D3 | AMBER | REAX | COMPASS | DREIDING | EFF |
|---|---|---|---|---|---|---|---|
| *a* (Å) | 6.89 | 6.81 | 7.21 | 6.87 | 6.99 | 6.97 | 6.90 |
| *b* (Å) | 9.51 | 9.43 | 9.37 | 9.17 | 9.21 | 9.59 | 9.37 |
| *c* (Å) | 6.58 | 6.51 | 6.46 | 6.46 | 6.32 | 6.48 | 6.84 |
| $\alpha$ (°) | 112.13 | 112.03 | 118.72 | 118.83 | 116.03 | 118.81 | 125.16 |
| $\beta$ (°) | 65.84 | 66.01 | 63.85 | 65.58 | 66.12 | 66.39 | 63.53 |
| $\gamma$ (°) | 108.90 | 108.57 | 110.43 | 109.51 | 111.12 | 111.38 | 108.90 |

Cyclohexane ($C_6H_{12}$)

| Lattice | Exp | DFT_D3 | AMBER | REAX | COMPASS | DREIDING | EFF |
|---|---|---|---|---|---|---|---|
| *a* (Å) | 11.23 | 11.11 | 11.12 | 10.93 | 10.60 | 11.11 | 11.21 |
| *b* (Å) | 6.44 | 6.43 | 6.49 | 6.82 | 6.53 | 6.62 | 6.83 |
| *c* (Å) | 8.20 | 8.11 | 8.13 | 8.06 | 8.68 | 7.94 | 8.07 |
| $\beta$ (°) | 108.83 | 109.14 | 109.74 | 105.92 | 107.02 | 106.23 | 109.24 |

Hexane ($C_6H_{14}$)

| Lattice | Exp | DFT_D3 | AMBER | REAX | COMPASS | DREIDING | EFF |
|---|---|---|---|---|---|---|---|
| *a* (Å) | 4.17 | 4.169 | 4.08 | 3.91 | 4.04 | 4.07 | 4.12 |
| *b* (Å) | 4.70 | 4.699 | 4.37 | 4.35 | 4.52 | 4.37 | 4.75 |
| *c* (Å) | 8.57 | 8.569 | 8.59 | 8.46 | 8.21 | 8.62 | 8.61 |
| $\alpha$ (°) | 96.60 | 96.597 | 97.36 | 99.40 | 96.12 | 97.25 | 98.60 |
| $\beta$ (°) | 87.20 | 87.198 | 88.01 | 87.67 | 88.63 | 87.76 | 86.44 |
| $\gamma$ (°) | 105.00 | 105.00 | 101.85 | 98.78 | 108.12 | 101.92 | 105.15 |

## Table S2: Lattice Constant *a* for Disordered Homochiral and Heterochiral Packed Stiff Chiral Nanothreads Candidates.

| Nanothread Type | Lattice Constant *a* for Homochiral Packing (Å) | Lattice Constant *a* for Hetero-chiral Packing (Å) |
|---|---|---|
| *Polytwistane*(*Stiffchiral-1*) | 6.38 | 6.36 |
| *Stiffchiral-2* | 6.90 | 6.86 |
| *Stiffchiral-3* | 6.89 | 6.85 |
| *Stiffchiral-4* | 6.73 | 6.65 |

## 6. Supplementary References


(1) Klotz, S.; Hamel, G.; Frelat, J. *High Press. Res.* **2004**, *24*, 219–223.
(2) Fang, J.; Bull, C. L.; Loveday, J. S.; Nelmes, R. J.; Kamenev, K. V. *Rev. Sci. Instrum.* **2012**, *83*, 093902.
(3) Fitzgibbons, T. C.; Guthrie, M.; Xu, E. S.; Crespi, V. H.; Davidowski, S. K.; Cody, G. D.; Alem, N.; Badding, J. V. *Nat. Mater.* **2015**, *14*, 43–47.
(4) Hrubiak, R.; Sinogeikin, S.; Rod, E.; Shen, G. Y. *Rev. Sci. Instrum.* **2015**, *86*, 072202.
(5) Piermarini, G. J.; Mighell, A. D.; Weir, C. E.; Block, S. *Science* **1969**, *165*, 1250–1255.
(6) Prescher, C.; Prakapenka, V. B. *High Press. Res.* **2015**, *35*, 223–230.
(7) Cornell, W. D.; Cieplak, P.; Bayly, C. I.; Gould, I. R.; Merz, K. M.; Ferguson, D. M.; Spellmeyer, D. C.; Fox, T.; Caldwell, J. W.; Kollman, P. A. *J. Am. Chem. Soc.* **1996**, *118*, 2309–2309.
(8) Blochl, P. E. *Phys. Rev. B* **1994**, *50*, 17953–17979.
(9) Kresse, G.; Joubert, D. *Phys. Rev. B* **1999**, *59*, 1758–1775.
(10) Perdew, J. P.; Burke, K.; Ernzerhof, M. *Phys. Rev. Lett.* **1996**, *77*, 3865–3868.
(11) Grimme, S.; Antony, J.; Ehrlich, S.; Krieg, H. *J. Chem. Phys.* **2010**, *132*, 154104.
(12) Grimme, S.; Ehrlich, S.; Goerigk, L. *J. Comput. Chem.* **2011**, *32*, 1456–1465.
(13) Kresse, G. *J. Non-Cryst. Solids* **1995**, *193*, 222–229.
(14) Kresse, G.; Furthmuller, J. *Comp. Mater. Sci.* **1996**, *6*, 15–50.
(15) Kresse, G.; Furthmuller, J. *Phys. Rev. B* **1996**, *54*, 11169–11186.
(16) Kresse, G.; Hafner, J. *Phys. Rev. B* **1994**, *49*, 14251–14269.
(17) Dresselhaus, M. S.; Dresselhaus, G.; Eklund, P. *Science of Fullerenes and Carbon Nanotubes: Their properties and Applications*, Elsevier, **1996**.
(18) Neumann, D. A.; Copley, J. R. D.; Kamitakahara, W. A.; Rush, J. J.; Cappelletti, R. L.; Coustel, N.; Fischer, J. E.; Jr., J. P. M.; III, A. B. S.; Creegan, K. M.; Cox, D. M. *J. Chem. Phys.* **1992**, *96*, 8631–8633.
(19) Lee, W. Y.; Slutsky, L. J. *J. Phys. Chem.* **1975**, *79*, 2602–2604.
(20) Breitling, S. M.; Jones, A. D.; Boyd, R. H. *J. Chem. Phys.* **1971**, *54*, 3959–3964.
(21) Kabo, G. J.; Blokhin, A. V.; Charapennikau, M. B.; Kabo, A. G.; Sevruk, V. M. *Thermochimica Acta* **2000**, *345*, 125–133.
(22) Chen, B.; Hoffmann, R.; Ashcroft, N. W.; Badding, J.; Xu, E. S.; Crespi, V. *J. Am. Chem. Soc.* **2015**, *137*, 14373–14386.
(23) Xu, E. S.; Lammert, P. E.; Crespi, V. H. *Nano Lett.* **2015**, *15*, 5124–5130.
(24) Olbrich, M.; Mayer, P.; Trauner, D. *J. Org. Chem.* **2015**, *80*, 2042–2055.
(25) Stojkovic, D.; Zhang, P. H.; Crespi, V. H. *Phys. Rev. Lett.* **2001**, *87*, 125502.
(26) Wen, X. D.; Hoffmann, R.; Ashcroft, N. W. *J. Am. Chem. Soc.* **2011**, *133*, 9023–9035.
(27) Toby, B. H.; Von Dreele, R. B. *J. Appl. Crystallogr.* **2013**, *46*, 544–549.
(28) Thiery, M. M.; Leger, J. M. *J. Chem. Phys.* **1988**, *89*, 4255–4271.
(29) Ciabini, L.; Santoro, M.; Gorelli, F. A.; Bini, R.; Schettino, V.; Raugei, S. *Nat. Mater.* **2007**, *6*, 39–43.
(30) Shinozaki, A.; Mimura, K.; Kagi, H.; Komatu, K.; Noguchi, N.; Gotou, H. *J. Chem. Phys.* **2014**, *141*, 084306.